Numerical simulation of miscible displacement processes in porous media flows under gravity

A. Rogerson
Center for Fluid Mechanics, Division of Applied Mathematics, Brown University, Providence, Rhode Island 02912

E. Meiburg
Department of Aerospace Engineering, University of Southern California, Los Angeles, California 90089-1191

(Received 12 April 1993; accepted 18 June 1993)

The nonlinear evolution of the interface between two miscible fluids of different densities and viscosities is simulated numerically for flow in a two-dimensional porous medium in which gravity is directed at various angles to the interface. Global velocities tangential to the interface are included in the analysis in addition to a normal displacing velocity. In unstable configurations, the viscous fingers that result translate as they amplify when nonzero tangential velocities are present. The increased stabilization by tangential shearing velocities reported in [A. Rogerson and E. Meiburg, Phys. Fluids A **5**, 1344 (1993)] affects the growth and wavelength selection of the emerging fingers. Tangential shearing also breaks the symmetry in the shape and concentration distribution of emerging fingers. In addition to the fingering mechanisms reported in previous studies, new mechanisms of diagonal fingering, trailing-lobe detachment, and secondary side-finger instability, resulting from the presence of gravity and tangential velocities, have been identified. These phenomena are reflected in one-dimensional averaged profiles of the concentration field. Also, how different density–concentration relations influence the interfacial evolution is investigated. When the dependence of viscosity and density on the concentration has different functional forms, the region of instability may be localized. The nature of the interfacial development is altered by varying the density relation and thereby changing the region of instability, suggesting that careful modeling of the density and viscosity relations is warranted.

I. INTRODUCTION

The unstable displacement flow of two fluids in a porous medium, or by analogy in a Hele–Shaw cell, has been studied extensively for 40 years. With applications in areas such as enhanced oil recovery and groundwater hydrology, this problem is of practical importance as well as of interest from a more classical fluid-dynamical point of view. An excellent review of the research on this problem for both miscible and immiscible displacements is provided by Homsy.[2] The unstable interface in the immiscible case develops into what is referred to as Saffman–Taylor fingers,[3] although the phenomenon was also reported by Hill[4] and the first formal stability analysis performed by Chuoke *et al.*[5] Considerably less attention has been directed towards the miscible problem even though it offers a rich array of interfacial dynamics. The majority of the work has focused on the stability and dynamics of the interface due to a normal displacement velocity. Tan and Homsy considered the case of neutrally buoyant fluids in a medium of constant permeability with isotropic dispersion, performing a linear stability analysis[6] as well as a numerical simulation of the nonlinear dynamics.[7] In the absence of gravitational forces, the dynamics of this flow is dictated by the viscosity contrast and the level of dispersion. The role of velocity-dependent dispersion on the stability of small-wavelength perturbations was later investigated by Yortsos and Zeybek.[8] The numerical study of Tan and Homsy was extended to include the affects of anisotropic dispersion,[9] permeability heterogeneity,[10] and velocity-dependent dispersion.[11] Some of the findings from these numerical simulations were confirmed in the first three-dimensional (3-D) experiment conducted by Bacri *et al.*[12] The effect of gravity was analyzed in the work of Bacri *et al.* but only at angles normal to the interface. A flow of two immiscible fluids that is of particular interest to our investigation is the one analyzed by Zeybek and Yortsos.[13,14] They studied the dynamics of interfaces parallel to the main flow direction, and found both theoretically and experimentally that the interface supports wave motions of a solitary nature.

The purpose of our investigation is to analyze the dynamics for the miscible case under gravity, directed at various angles with respect to the interface, and including global velocities tangential to the interface in addition to the normal displacement velocity typically taken. We focus on these aspects and consider the isotropic-dispersion constant-permeability case. The linear stability of this flow was analyzed by the authors.[1] A new criterion for instability was formulated that incorporated gravitational effects due to density contrast. Unlike immiscible displacement processes, it was found that the presence of tangential shearing velocities increases the stability of the flow. The linear theory also shows that the presence of global tangential velocities results in traveling wave solutions. We are interested in the nonlinear evolution of these waves which amplify when the flow is viscously or gravitationally un-

 0899-8213/93/5(11)/2644/17/$6.00

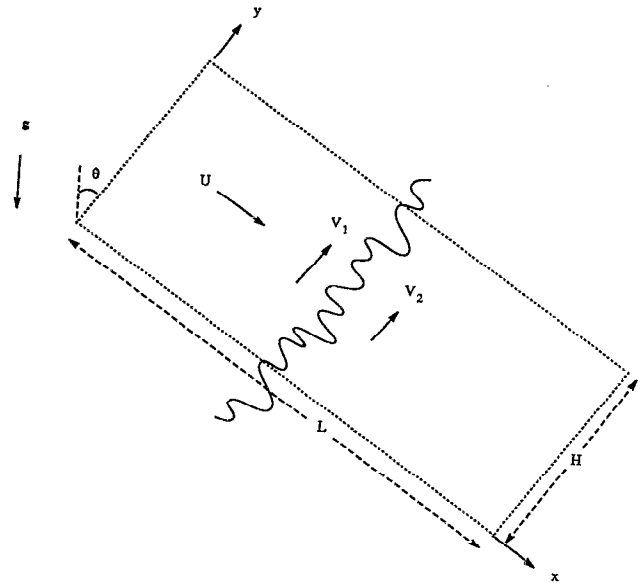

FIG. 1. Flow configuration. The interface is aligned along the y axis. U is a global displacement velocity normal to the interface in the x direction, while V_1 and V_2 are velocities tangential to the interface. The angle between the interface and gravity is denoted by θ. The domain has length L in the x direction and width H in the y direction.

stable due to the normal displacing velocity. The addition of tangential velocities also presents the possibility for new fingering mechanisms and instabilities. Furthermore, the addition of buoyancy forces allows us to investigate flows where viscous effects and density effects dominate in different parts of the mixing zone, creating localized regions of instability.

II. FORMULATION

A. Governing equations

We consider the two-dimensional configuration of a porous medium in which two incompressible fluids of different densities and viscosities are separated by a diffusing interface or mixing zone. We introduce a coordinate system with y axis parallel to the interface, and x axis normal to it (Fig. 1). U represents a global displacement velocity normal to the interface, directed from fluid 1 to fluid 2, while V_1 and V_2 denote the respective fluid velocity components tangential to the interface. Gravity is aligned at various angles θ to the interface. We assume that the medium is of constant permeability k and the dispersion is isotropic, with constant diffusion coefficient D.

The governing equations for this flow are,

$$\nabla\cdot\mathbf{u}=0, \tag{1}$$

$$\nabla p=-\frac{\mu}{k}\mathbf{u}+\rho\mathbf{g}, \tag{2}$$

$$\frac{\partial c}{\partial t}+\mathbf{u}\cdot\nabla c=D\nabla^2 c. \tag{3}$$

The above equations express the conservation of mass, momentum (Darcy's law), and species, with c denoting the concentration of fluid 1. Both the viscosity and the density are assumed to be known functions of the concentration

$$\mu=\mu(c), \quad \rho=\rho(c). \tag{4}$$

We consider a finite domain and use the boundary conditions

$$\begin{aligned} &c=c_1=1, \quad \mathbf{u}=(U,V_1) \quad \text{at } x=0,\\ &c=c_2=0, \quad \mathbf{u}=(U,V_2) \quad \text{at } x=L, \end{aligned} \tag{5}$$

and

$$(\mathbf{u},c)(x,y=0,t)=(\mathbf{u},c)(x,y=H,t). \tag{6}$$

Following Tan and Homsy, we introduce the velocity, length and time scales U, D/U, and D/U^2. By furthermore scaling viscosity, density, and pressure by μ_1, ρ_1, and $\mu_1 D/k$, respectively, we obtain the set of dimensionless equations

$$\nabla^*\cdot\mathbf{u}^*=0, \tag{7}$$

$$\nabla^* p^*=-\mu^*\mathbf{u}^*+G\rho^*(\sin\theta,-\cos\theta), \tag{8}$$

$$\frac{\partial c^*}{\partial t^*}+\mathbf{u}^*\cdot\nabla c^*=\nabla^{*2}c^*, \tag{9}$$

with boundary conditions,

$$\begin{aligned} &c^*=1, \quad \mathbf{u}^*=(1,V_1^*) \quad \text{at } x^*=0,\\ &c^*=0, \quad \mathbf{u}^*=(1,V_2^*) \quad \text{at } x^*=\mathrm{Pe}A, \end{aligned} \tag{10}$$

$$(\mathbf{u}^*,c^*)(x^*,0,t^*)=(\mathbf{u}^*,c^*)(x^*,\mathrm{Pe},t^*). \tag{11}$$

Here, $G=(\rho_1 g k)/(\mu_1 U)$ is a dimensionless parameter describing the relative importance of gravitational and viscous effects, $\mathrm{Pe}=UH/D$ is the Péclet number, and $A=L/H$ is the aspect ratio of the domain. These equations admit the base-flow solution

$$u_b(x,t)=1, \tag{12}$$

$$v_b(x,t)=-\frac{1}{\mu_b}[\eta(t)+G\rho_b(x,t)\cos\theta], \tag{13}$$

$$p_b(x,t)=\int^x[-\mu_b(\zeta,t)+G\rho_b(\zeta,t)\sin\theta]d\zeta+y\eta(t), \tag{14}$$

$$c_b(x,t)=\frac{1}{2}\operatorname{erfc}\left(\frac{x-t}{2\sqrt{t}}\right), \tag{15}$$

$$\mu_b=\mu_b(c_b)=\mu_b(x,t), \tag{16}$$

$$\rho_b=\rho_b(c_b)=\rho_b(x,t). \tag{17}$$

Here, $\eta(t)$ is an arbitrary function of time only, indicating that for a given flow configuration, there are infinitely many v-velocity base states possible. Notice that this base-flow differs from the one given in the stability analysis of this flow[1] only in that here c refers to the concentration of fluid 1, while in Ref. 1 c refers to the concentration of fluid 2.

If we now consider a reference frame moving in the x^* direction with the uniform flow $u^*=1$ and in the y^* direction with the average tangential velocity $v^* = V_0^*$, and use the streamfunction-vorticity formulation

$$u=\psi_y, \quad v=-\psi_x, \tag{18}$$

then the equations become (dropping the *s),

$$c_t+\psi_y c_x-\psi_x c_y=c_{xx}+c_{yy}, \tag{19}$$

$$\omega=\frac{1}{\mu}\frac{d\mu}{dc}[(\psi_x-V_0)c_x+(\psi_y+1)c_y]-\frac{G}{\mu}\frac{d\rho}{dc} \times(\cos\theta\, c_x+\sin\theta\, c_y), \tag{20}$$

$$\nabla^2\psi=-\omega, \tag{21}$$

with boundary conditions,

$$\begin{aligned} &c=1, \quad \psi_y=0, \quad \psi_x=-V_1+V_0 \quad \text{at } x=-t, \\ &c=0, \quad \psi_y=0, \quad \psi_x=-V_2+V_0 \quad \text{at } x=\mathrm{Pe}\,A-t, \end{aligned} \tag{22}$$

$$(\psi,c)(x,-V_0t,t)=(\psi,c)(x,\mathrm{Pe}-V_0t,t). \tag{23}$$

For the majority of the results presented here, we use viscosity and density relationships in keeping with our earlier work on the stability of the interface,[1]

$$\mu(c)=e^{R(1-c)}, \quad \rho(c)=e^{S(1-c)}, \tag{24}$$

yielding,

$$c_t+\psi_y c_x-\psi_x c_y=c_{xx}+c_{yy}, \tag{25}$$

$$\omega=-R[(\psi_x-V_0)c_x+(\psi_y+1)c_y]+GSe^{(S-R)(1-c)} \times(\cos\theta c_x+\sin\theta c_y), \tag{26}$$

$$\nabla^2\psi=-\omega. \tag{27}$$

B. Numerical method

The solution to Eqs. (25)–(27) is approximated numerically using a Fourier Galerkin method. The use of the Fourier projection requires that we cast the problem in a periodic setting. In the transverse direction, this is no problem as we have already assumed periodic boundary conditions in the formulation. In the longitudinal direction, we follow the approach of Tan and Homsy[7] and achieve periodicity by incorporating a periodic extension of the concentration field on the right of the computational domain. We shall focus on the dynamics of the interface on the left for unstable parameter sets, and stop the simulation before fingering is influenced by the right interface which is stable.

The Fourier expansion of the functions c, ψ, and ω is

$$(c,\psi,\omega)(x,y,t)=\sum_{j=-M/2}^{M/2-1}\sum_{l=-N/2}^{N/2-1}(\hat{c},\hat{\psi},\hat{\omega}) \times(k_j^x,k_l^y,t)e^{ik_j^x x}e^{ik_l^y y}, \tag{28}$$

where $k_j^x=2\pi j/\mathrm{Pe}A$ and $k_l^y=2\pi l/\mathrm{Pe}$ are the wave numbers in the x and y directions. At the equally spaced grid points given by

$$\begin{aligned} &x_m=(\mathrm{Pe}A/M)m \quad \text{for } m=0,\cdots,M-1, \\ &y_n=(\mathrm{Pe}/N)n \quad \text{for } n=0,\cdots,N-1, \end{aligned} \tag{29}$$

the transform coefficients (and the inverse transform) can be obtained from fast Fourier transforms (FFTs). Equations (25)–(27) are recast into equivalent equations for the expansion coefficients. Fourier coefficients for the nonlinear terms are found in the usual manner, by computing the nonlinear term at the physical grid points (x_m,y_n) and then transforming to Fourier space. We also apply a weak exponential cutoff filter (cf. Ref. 15) to the transformed Poisson equation [Eq. (27)]

$$\hat{\psi}_{jl}=\frac{\hat{\omega}_{jl}}{(k_j^x)^2+(k_l^y)^2}\sigma(\vartheta_j^x)\sigma(\vartheta_l^y), \tag{30}$$

where

$$\sigma(\vartheta)=\begin{cases}1 & \text{for } |\vartheta|\leqslant\vartheta^c, \\ \exp[-\alpha(|\vartheta|-\vartheta^c)^8] & \text{for } \vartheta^c\leqslant|\vartheta|\leqslant\pi,\end{cases} \tag{31}$$

with $\vartheta_j^x=2\pi j/M$ and $\vartheta_l^y=2\pi l/N$, which provides a bit of control over the high modes. We take $\alpha=37$, since e^{-37} is the order of machine accuracy, and $\vartheta^c=0.6\pi$. The computation is advanced in time in Fourier space using a low-storage third-order total variation diminishing (TVD) Runge–Kutta scheme.[16]

III. RESULTS

In all of the cases we present, the interface is viscously unstable ($R>0$), with a less viscous fluid (fluid 1) displacing a more viscous fluid (fluid 2). The fluids may be stably or unstably stratified with respect to buoyancy forces, but we are interested in the evolution of an interface which is, overall, unstable. In Ref. 1 we formulated an instability criterion for the interface given by

$$R-GS\sin\theta\frac{(1+e^S)}{(1+e^R)}>0, \tag{32}$$

where $R=\ln(\mu_2/\mu_1)$, $S=\ln(\rho_2/\rho_1)$, $G=(g\rho_1)/(U\mu_1)$ and θ is the angle of inclination.

To encourage the destabilization of the interface, a perturbation is added to the initial concentration field

$$c_0(x,y)=c_b(x)+c'(x,y). \tag{33}$$

Since a sharp interface will induce the Gibbs phenomenon, a smooth error function profile is used for the base-flow concentration

$$c_b(x,t_0)=\frac{1}{2}\left[1+\mathrm{erfc}\left(\frac{x-x_1}{2\sqrt{t_0}}\right)+\mathrm{erf}\left(\frac{x-x_2}{2\sqrt{t_0}}\right)\right], \tag{34}$$

where $t_0>0$ is some initial starting time, x_1 is the location of the front of interest and x_2 is the location of the stable periodic front. Generally, t_0 is chosen so that six grid points are between $c_0=0.025$ and $c_0=0.975$. The v-velocity base flow is given by

$$v_b(x,t_0)=-e^{-R(1-c_0)}[\eta(t_0)+Ge^{S(1-c_0)}\cos\theta], \tag{35}$$

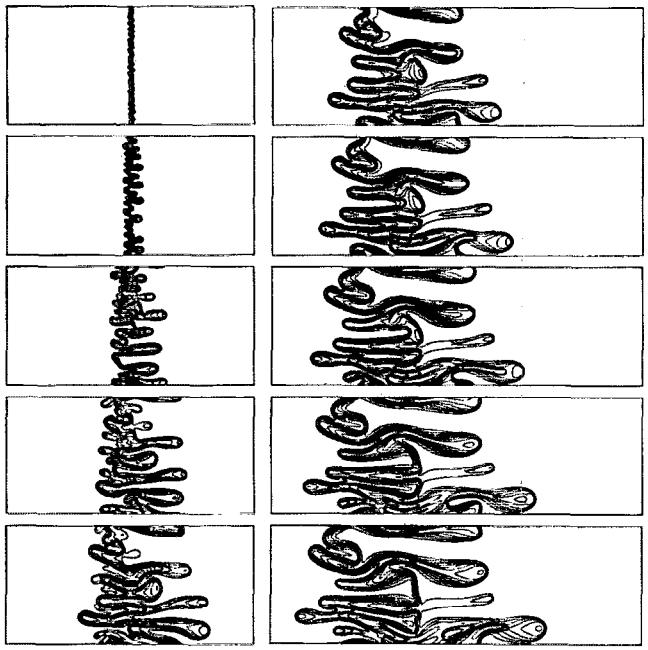

FIG. 2. Concentration contours for Pe=1000, $R=3$, $S=0$, $V_1=V_2=0$ showing a representative horizontal fingering pattern when no tangential velocities are present. Frames correspond to $t=100$, 200, 400, 600, 800, 1000, 1100,...,1400.

where $\eta(t_0)$ is arbitrary. We select an η by specifying the average v velocity, V_0, with which the reference frame moves in the y direction. Then η, and consequently v_b, are determined from the relation

$$\frac{1}{\mathrm{Pe}A}\int_0^{\mathrm{Pe}A} v_b(x,t_0)\,dx=V_0. \tag{36}$$

The streamfunction is then initialized so that

$$\frac{\partial\psi_0}{\partial y}=u_b(x,t_0)=0, \tag{37}$$

$$\frac{\partial\psi_0}{\partial x}=-v_b(x,t_0)+V_0. \tag{38}$$

In the presentation that follows, we illustrate the interface by plotting concentration contours at levels $c=0.1$, 0.2,..., 0.9. In the interest of space, only the flowfield of interest will be shown, so the periodic front will not be displayed and some frames may be clipped more than others. Unless otherwise noted the results are shown in the reference frame moving with velocity (U,V_0), and in some cases for clarity we will show 2 periods in the y direction.

A. Summary of fingering mechanisms in the absence of tangential shear

When there are no buoyancy forces and no tangential velocities, the unstable interface evolves into horizontal fingers that interact with each other. An example of the interfacial development is shown in Fig. 2 for Pe=1000 and $R=3$. When the fingers are first visible in frame 1, there appear to be approximately 17 fingers with an average wavelength of $\lambda=\mathrm{Pe}/17=58.8$. This agrees well with the most unstable wavelength predicted by the linear theory at this time, $\lambda_{\max}=61.3$. Later in the next section we will make more specific comparisons between the linear stability results and the growth rate of perturbations calculated from the simulated flow. The various mechanisms that characterize the dynamics of the fingers shown in Fig. 2 are summarized in Zimmerman and Homsy.[9] Throughout the simulation the *shielding* and *pairing* mechanisms act to reduce the number of fingers and increase the lateral scale of the fingers. A shielding finger is one that grows slightly ahead of its neighbors. The concentration gradients of this finger steepen allowing it to advance even further ahead and spread, shielding the neighboring fingers and inhibiting their growth. Eventually, the shielded finger collapses, changing the width of the dominating finger as it pairs with the shielded one. The mechanisms of *fading* and *coalescence* were first observed in the anisotropic dispersion simulations of Zimmerman and Homsy.[9] Later, Zimmerman and Homsy in Ref. 11 found that these mechanisms also occur in isotropic simulations with high Pe number. (We remark that Zimmerman and Homsy use the characteristic length L, instead of H, to define the Péclet number.) These mechanisms are also evident in our simulations. Examples of fading can be seen in Fig. 2, frames 3 and 6, where a finger that has grown and advanced into fluid 2, fades in concentration as fluid 1 flows instead through the shorter adjacent fingers. In frame 3, the coalescence mechanism is also observed. Zimmerman and Homsy[9] describe coalescence as the tip of a finger bending into the body of an adjacent finger and merging with it. In frame 3, we see a finger that spreads at the tip and then merges with the adjacent finger, rather than "bend" into it, but completely coalesces eventually. A similar event occurs in frame 6, but as the tip spreads and the gradient steepens, the tip splits (frame 7) and only part of the finger coalesces with the adjacent finger. This process is repeated in frames 9 and 10.

B. Effect of tangential shear on emerging fingers

We now begin to investigate the effects of gravity and tangential velocities on the growth and development of the interface. In Ref. 1 we presented results from a linear hydrodynamic stability analysis for this flow. In this analysis, we found that when there is a tangential velocity difference across the front, the stability of the flow is increased. Unlike immiscible displacement processes where the presence of tangential velocities does not alter the growth rate and affects only the phase speed of the perturbations, in the miscible case considered here the stability of the flow can be significantly increased by tangential shear. We compare these results with growth rates computed from the early evolution of the simulated flow field. By employing the quasi-steady-state approximation (QSSA) in the linear stability analysis, we assumed that the rate of change of the base state is small compared to the growth rate of the perturbations. Since the rate of change of the base state is $t^{-3/2}$, we expect the theoretical growth rates to approximate those from the simulation for times $t\gg 1$.

In Fig. 3 the growth rates for a representative case are plotted as a function of time. The perturbation concentra-

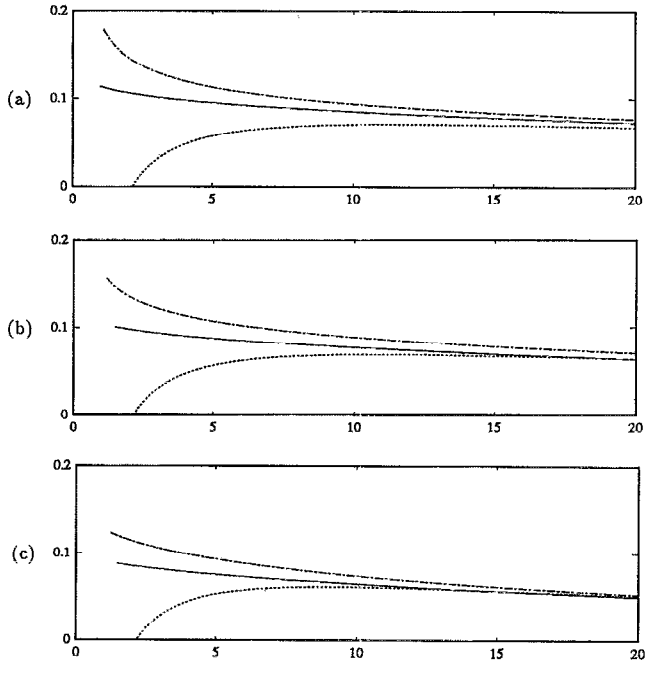

FIG. 3. Growth rates as a function of time for $R=3$, $S=-2$, $G=1$, $\theta=\pi/2$, and $k=0.15$. Solid curve: theoretical QSSA results; Dot–dot curve: simulation results from rms concentration perturbation; Dot–dash curve: simulation results from rms u-velocity perturbation. (a) $V_1=V_2=0$, (b) $|V_1-V_2|\approx 1-e^{-R}$, (c) $|V_1-V_2|\approx 2(1-e^{-R})$.

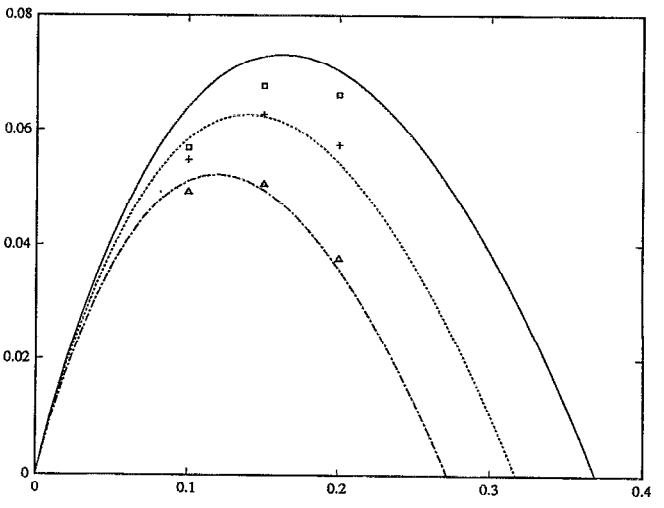

FIG. 4. Growth rate versus wave number for $R=3$, $S=-2$, $G=1$, $\theta=\pi/2$ at time $t=20$. Curves correspond to theoretical results: $V_1=V_2=0$ (solid), $|V_1-V_2|\approx 1-e^{-R}$ (dot–dot), $|V_1-V_2|\approx 2(1-e^{-R})$ (dot–dash). Symbols correspond to the simulation results from the rms concentration perturbation: $V_1=V_2=0$ (square), $|V_1-V_2|\approx 1-e^{-R}$ (cross), $|V_1-V_2|\approx 2(1-e^{-R})$ (triangle).

tion is initialized as a single-wavelength cosine of amplitude $\epsilon=0.001$ in the y direction weighted with a Gaussian in the x direction

$$c'(x,y,t_0)=-\epsilon\cos\left(\frac{2\pi y}{\mathrm{Pe}}\right)e^{-(x-x_1)^2/(4t_0)}. \tag{39}$$

The results for wave number $k=2\pi/\mathrm{Pe}=0.15$ are shown in Fig. 3(a) for the case with no tangential shearing, with Figs. 3(b) and 3(c) corresponding to increasingly stronger tangential shear strength. The growth rate at subsequent times is computed from both the rms concentration perturbation and the rms u-velocity perturbation and is plotted along with the theoretical results from the stability analysis. We see that the growth rates computed from the simulation asymptotically approach the theoretical rates as time increases, validating the use of the QSSA approach. Growth rates for $k=0.10$ and $k=0.20$ were computed in a similar manner. These results are compiled in Fig. 4, showing the growth rate as a function of wave number at time $t=20$ for the three tangential shear strengths. As reported in Ref. 1, both the growth rate and range of unstable wave numbers decrease as the strength of the tangential shear increases.

The increased stabilization by tangential shear affects the growth and wavelength selection of the emerging fingers. As an example, consider a set of simulations with $\mathrm{Pe}=500$, $R=3$, $S=0$, and three sets of tangential shearing velocities. Figure 5 shows the fingers that begin to appear from an initial concentration field that has been perturbed with random noise of magnitude 0.1. This initial condition allows the most unstable wavelength to emerge. As the strength of the shear increases, the flow becomes more stable and the growth of fingers is retarded. In addition, fewer fingers with larger lateral scale emerge as the shear increases due to the shift in the most dangerous mode to longer wavelengths. Both of these effects can be seen more clearly in Fig. 6, where a one-dimensional slice of the concentration field through the front is plotted at time $t=100$. The quadrupolelike perturbation vorticity structure that was found in Ref. 1 to be the cause of the increased stabilization, is also evident in our simulations. In Fig. 7, contours of the perturbation vorticity for the three cases discussed above show the dipolelike structure for the no-shear case and quadrupolelike structures for the shearing cases. The dipolelike structure is similar to ones illustrated in the numerical simulations of Zimmerman and Homsy.[9] In a different context, Manickam and Homsy[17] have observed quadrupolelike structures due to nonmonotonicities in the viscosity profile.

The presence of tangential shearing velocities also affects the shape and concentration distribution of the emerging fingers. As an example, a series of simulations for $\mathrm{Pe}=250$, $R=3$, and $S=0$ is shown in Fig. 8 where the interface is perturbed with a cosine wave so that a single finger develops. The first row corresponds to $V_1=V_2=0$ and the subsequent rows show the results for increasing tangential shear $|V_1-V_2|=V_1(1-e^{-R})$, with V_1 in the $+y$ direction. In the first column we see that when there is no tangential shear the finger is symmetric, and the steepest part of the interface is centered about the finger tip. As the strength of the shear increases, the finger loses its symmetry and the steepest region of the interface shifts to the upper side of the finger. The concentration gradient becomes steep in response to the cross-flow that stretches the interface. In Fig. 9, streamlines in a stationary reference

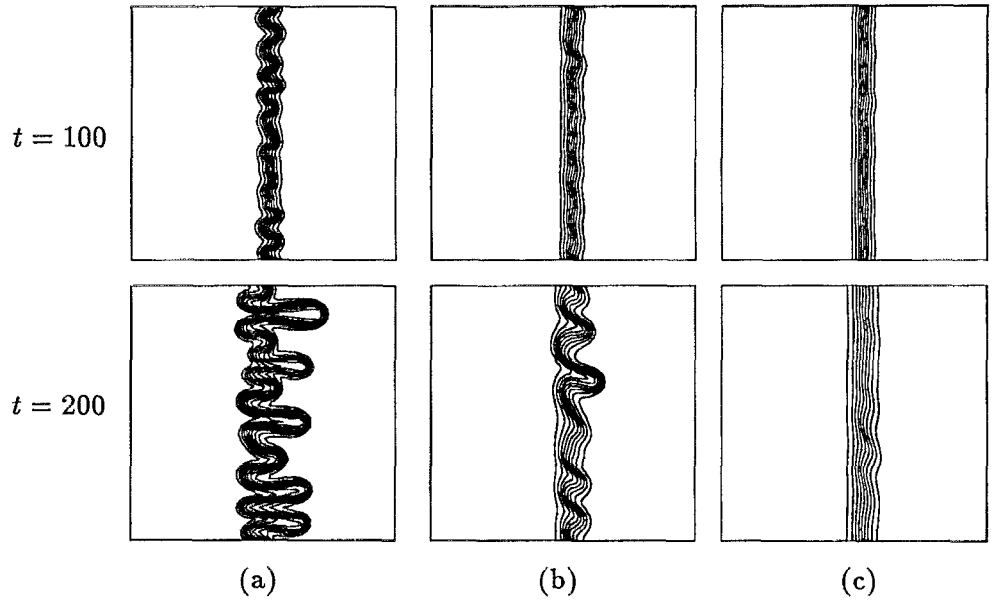

FIG. 5. Concentration contours for Pe=500, $R=3$, $S=0$ at $t=100$ and $t=200$ for three tangential shearing velocities. (a) $V_1=V_2=0$, (b) $|V_1-V_2|=2.5(1-e^{-R})$, (c) $|V_1-V_2|=5.0(1-e^{-R})$. As the shearing strength increases, the lateral scale of the fingers increases and their growth is slowed.

frame corresponding to time $t=200$ show how the region of stretching shifts from the center of the tip to the upper side of the finger as the strength of the shear increases. The loss of symmetry is further illustrated at later times (columns 2 and 3 of Fig. 8). The no-shear case undergoes a classical *tip-splitting* event. As Tan and Homsy discuss in Ref. 7, in order for the tip to split, it must spread wide enough to allow two wavelengths of an unstable perturbation to grow. At the same time, the front must steepen, amplifying the perturbations and forcing the tip to destabilize. When tangential velocities are present, the split is no longer symmetric. As the regions of maximum concentration variation shift to the upper side of the finger, the upper lobe is favored over the lower lobe, amplifying the perturbation there more quickly. The contrast in steepness across the tip is so great when $V_1=2.5$ (last row), that the per-

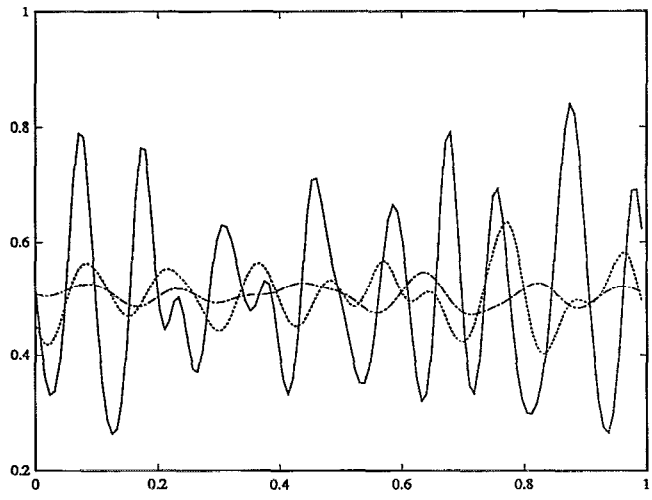

FIG. 6. Concentration variation at the center of the front at $t=100$ for the simulation in Fig. 5. $V_1=V_2=0$ (solid curve), $|V_1-V_2|=2.5(1-e^{-R})$ (dot–dot), $|V_1-V_2|=5.0(1-e^{-R})$ (dot–dash).

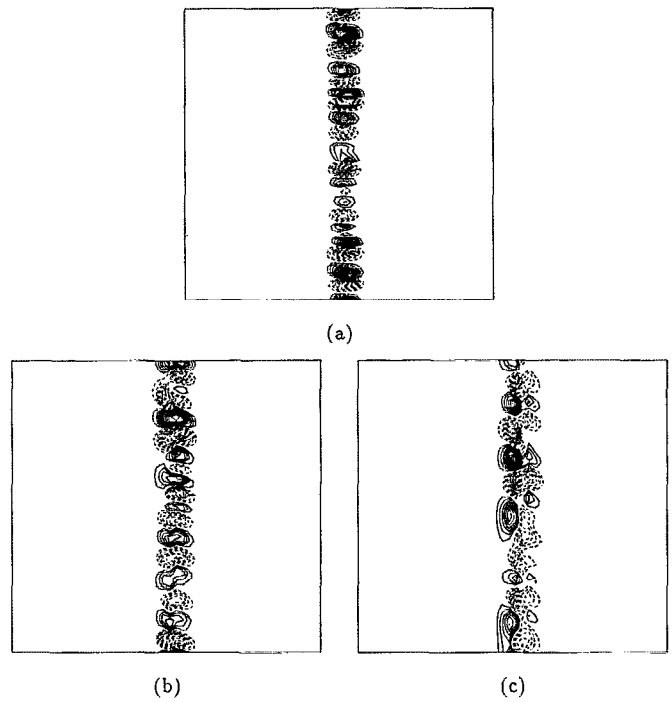

FIG. 7. Perturbation vorticity at $t=100$ for the simulation in Fig. 5. (a) $V_1=V_2=0$, (b) $|V_1-V_2|=2.5(1-e^{-R})$, (c) $|V_1-V_2|=5.0(1-e^{-R})$. The no-shear case, (a), exhibits a dipolelike structure. The weak-shear case, (b), shows a tendency towards the quadrupolelike structure that is more prominent in the strongly sheared case, (c).

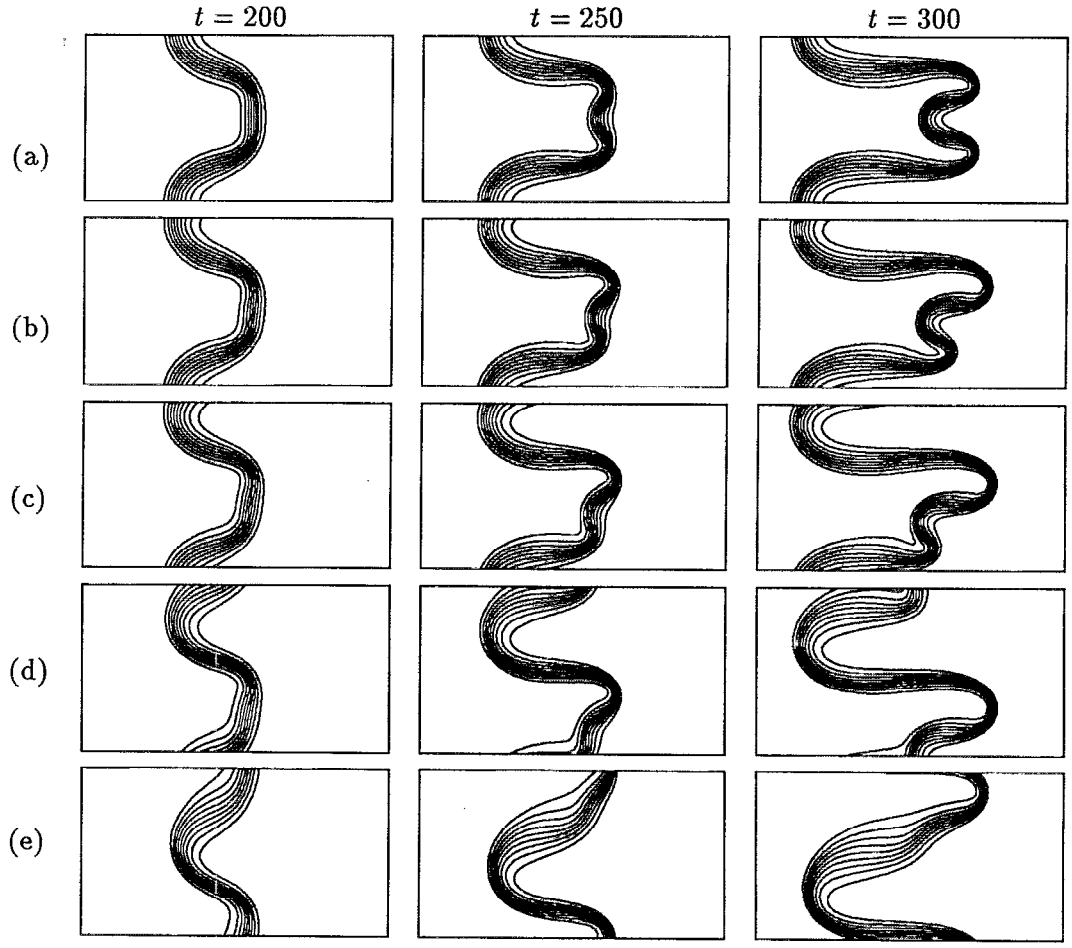

FIG. 8. Concentration contours for Pe=250, $R=3$, $S=0$, and various tangential shear strengths $|V_1-V_2|=V_1(1-e^{-R})$. (a) $V_1=0$, (b) $V_1=0.25$, (c) $V_1=0.50$, (d) $V_1=1.25$, (e) $V_1=2.5$. Tangential velocity shear breaks the symmetry in the shape and concentration distribution of emerging fingers.

turbation on the under side is barely observed. In this case a single asymmetrical finger with steep gradient on the upper side has developed. Notice also that we begin to see the steepening of the back or "root" of the finger in the tangential shearing cases. We will discuss this further in the next section.

C. New fingering mechanisms

In addition to the fingering mechanisms that have been reported before, new dynamics are possible due to the presence of gravity and tangential velocities. In particular, with velocities tangential to the interface in addition to the velocity $U=1$ normal to it, it seems possible to obtain *diagonal fingering*. Figure 10 shows an example of this situation in which $(V_1,V_2)=(-1.28,-2.73)$ with Pe=500, $R=3$, $S=4$, $G=1$, and $\theta=0$. When there are global tangential velocities, the linear perturbations on the interface travel with a nonzero phase speed. Unless the global v velocity about the finger is approximately equal to this phase speed, some degree of diagonal fingering will occur. For the case in Fig. 10, the phase speed is approximately -2.42. The interface in Fig. 10 is displayed in the reference frame moving in the y direction with the average v velocity $V_0=-2.0$ so the fingers appear to be translating more slowly. To illustrate the diagonally directed fingering, streamfunction contours are shown in Fig. 11 in a reference frame that is stationary in the x direction and moving in the y direction with the phase speed of the perturbations. In this case, the v-velocity field about the finger is negative with magnitude greater than the magnitude of the phase speed, so the finger grows diagonally in the $-y$ direction.

The presence of nonzero tangential velocities can also lead to secondary instabilities of the fingers. These instabilities are illustrated in Fig. 12 which shows the evolution of a single finger resulting from the initial concentration perturbation

$$c'(x,y,t_0)=-0.1\cos\left(\frac{2\pi y}{\mathrm{Pe}}\right)e^{-(x-x_1)^2/(4t_0)}. \tag{40}$$

Two periods in the y direction are shown. Here, Pe=500, $R=3$, $S=1$, $G=1$, $\theta=0$ and the induced tangential velocity is such that $(V_1,V_2)=(-4.5,-0.3)$. As we saw before, the shape of the initial finger is influenced by tangential velocities. The strong tangential shearing from $V_1=-4.5$ to $V_2=-0.3$ results in steep concentration gradients on the under side of the growing perturbation (frame 1). This

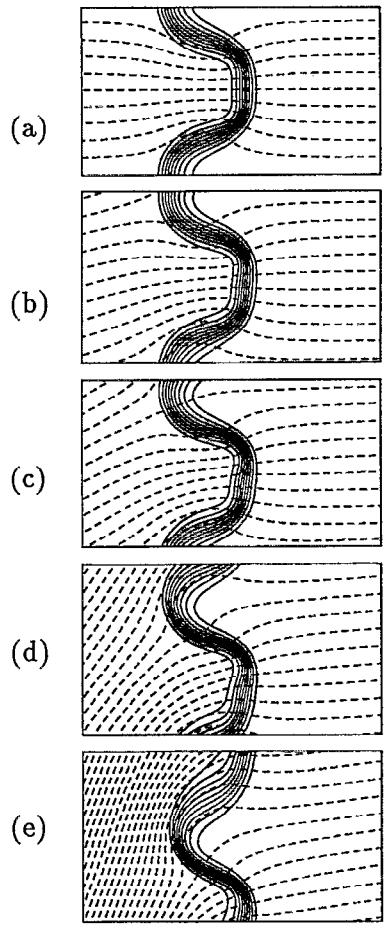

FIG. 9. Streamfunction contours in a stationary reference frame, along with the corresponding concentration contours, for Pe=250, $R=3$, $S=0$, and various tangential shear strengths $|V_1-V_2|=V_1(1-e^{-R})$ at $t=200$. (a) $V_1=0$, (b) $V_1=0.25$, (c) $V_1=0.50$, (d) $V_1=1.25$, (e) $V_1=2.5$. As $|V_1-V_2|$ increases, the region of steep concentration gradient shifts to the upper side of the finger in response to interfacial stretching.

concentration distribution strongly favors the growth of the lower lobe in frame 2, which quickly shields the growth of the other lobe. By frame 3, a single asymmetrical finger has developed, with one side steeper than the other. This finger develops horizontally since the v velocity about the finger matches the phase speed. Because the sides of the finger are subject to global v velocities and are exposed to a gravitational field, these regions of the interface may go unstable. In this configuration, with both gravity and the displacing v velocity aligned in the $-y$ direction perpendicular to the finger sides, the upper side is viscously stable and gravitationally unstable since the displacing velocity and gravity are directed from the heavier, more viscous fluid (fluid 2) to the lighter, less viscous fluid (fluid 1). Similarly, the under side is viscously unstable and gravitationally stable. The criterion for the overall instability of an interface subject to a normal displacement velocity V directed from fluid "a" to fluid "b" is

$$V(\mu_a+\mu_b)(\ln\mu_b-\ln\mu_a) - g\sin\theta(\rho_a+\rho_b)(\ln\rho_b-\ln\rho_a)>0 \tag{41}$$

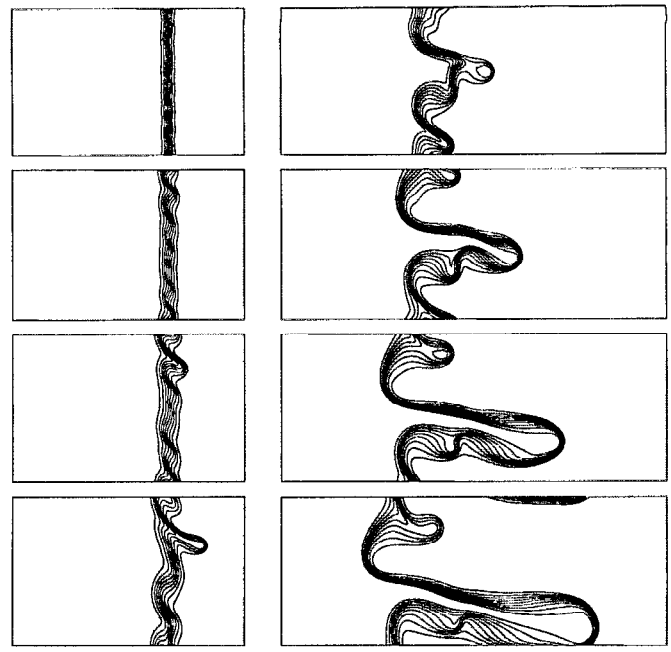

FIG. 10. Concentration contours for Pe=500, $R=3$, $S=4$, $G=1$, $\theta=0$, $(V_1,V_2)=(-1.28,-2.73)$ showing diagonally directed fingers. Frames correspond to $t=100, 200,...,800$.

in dimensional form (cf. Ref. 1). With respect to the finger sides in this example, the angle θ is $\pi/2$ since gravity is aligned with the displacing velocity. Equation (41) then specifies a critical condition for instability on the finger sides. For the upper side, V is directed from fluid 2 to fluid 1 and the nondimensional instability criterion becomes

$$|V|<\frac{GS(1+e^S)}{R(1+e^R)}, \tag{42}$$

while the under side has V directed from fluid 1 to fluid 2 yielding

$$|V|>\frac{GS(1+e^S)}{R(1+e^R)} \tag{43}$$

for instability. In this case, the magnitude of both V_1 and V_2 are greater than the critical velocity

$$V_{\text{crit}}=\frac{GS(1+e^S)}{R(1+e^R)}=0.0588, \tag{44}$$

so the upper side is stable while the under side is unstable. The first instability that we see in Fig. 12 develops at the

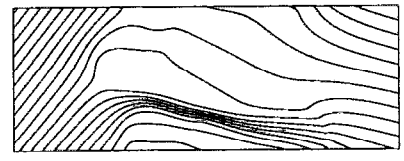

FIG. 11. Streamfunction contours corresponding to the last time frame in Fig. 10. The reference frame is stationary in the x direction and moving in the y direction with the phase speed of the perturbations.

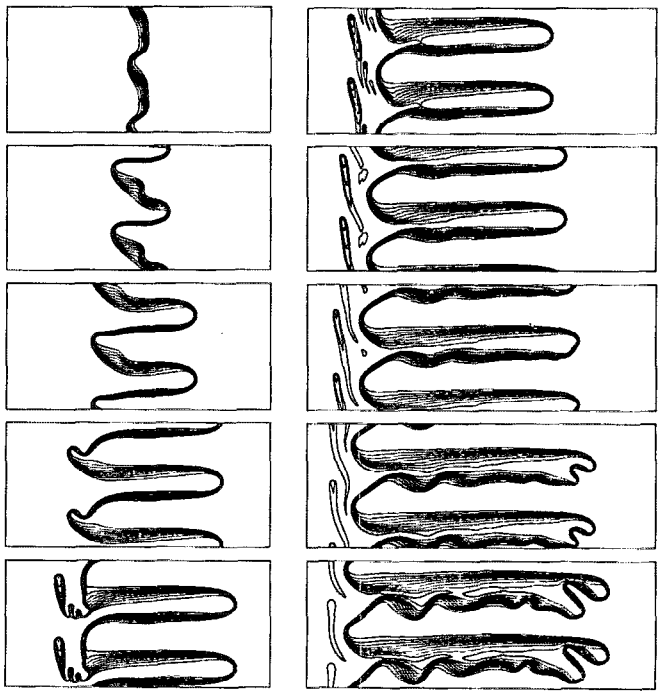

FIG. 12. Concentration contours for Pe=500, $R=3$, $S=1$, $G=1$, $\theta=0$ $(V_1,V_2)=(-4.5,-0.3)$ showing trailing-lobe detachment and side-finger instability. Two periods in the y direction are displayed. Frames correspond to $t=400$, 600, 800, 1000, 1100, 1200,...,1600.

root of the finger. In frame 4, a lip forms and goes unstable in response to the velocity $V_1=-4.5$, forming a trailing lobe. Fluid 1 fingers through this part of the interface with relatively small wavelength (frame 5) since the displacing velocity, V_1, is comparatively large. The fingering quickly breaks through both fronts (frame 6), leaving blobs of the more viscous fluid to diffuse into the surrounding fluid 1. We refer to this process as *trailing-lobe detachment*. Notice that in frame 6, the gradient of each finger side is approximately the same, while the region at the root of the under side has remained steep. An instability on the under side of the finger due to the velocity $V_2=-0.3$ also becomes visible (frames 6 and 7). Since V_2 is small, the growth is slow and the wavelength of the perturbation is large. As this secondary *side-finger instability* grows, it assists in widening the tip of the finger (frame 8) which encourages a tip-splitting event (frame 9). As expected, the upper side of the finger is stable. In frame 10 we see another lip beginning to form at the root of the finger, and we expect that another trailing-lobe detachment will occur.

Throughout this simulation, the under side of the back of the finger remains a region of steep concentration gradient. Although the finger emerged with steep gradients all along the under side, the back end or root, like the tip, must undergo continued stretching to maintain the sharp concentration gradients. The root, like the tip, is stretched by local cross-flow, but the root is also subject to stretching from the tangentially shearing base flow. To illustrate, base-state streamfunction contours corresponding to this simulation are shown in Fig. 13 in a stationary frame of

FIG. 13. Base-state streamfunction contours in a stationary reference frame where $U=1$ and $(V_1,V_2)=(-4.5,-0.3)$. Stretching of the interface due to the base-flow velocity field causes persistent steep gradients at the root of the finger.

reference. Since the vertical cross section of these streamtubes is constant, a purely vertical section of the interface would not be stretched by the base-flow velocity field. For example, the unperturbed 1-D vertical interface is not stretched and therefore does not steepen. However, a horizontal section of the interface or one angled diagonally (with positive slope), would be stretched as the cross section of the streamtubes taken in this direction widen from phase 1 to phase 2. It is this stretching mechanism that is primarily responsible for the steep gradients that persist on the under side of the root of the finger in Fig. 12. In all cases with sufficient tangential shear, steep gradients will appear at the back of the fingering interface in the vicinity of the base-flow tangential velocity transition. The side that steepens depends on the direction and relative magnitudes of V_1 and V_2 and can be explained by simply considering the stretching of the interface by the global velocity field.

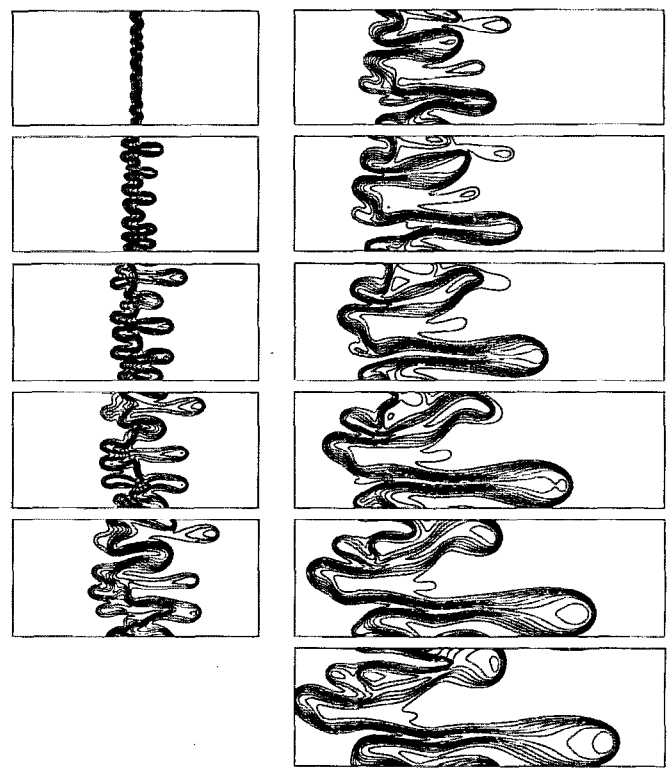

FIG. 14. Concentration contours for Pe=500, $R=3$, $S=0$, and no tangential velocity shear, $V_1=V_2=0$. The horizontal fingering pattern illustrates the shielding, pairing, fading, and coalescence mechanisms. Frames correspond to $t=100$, 200,...,1100.

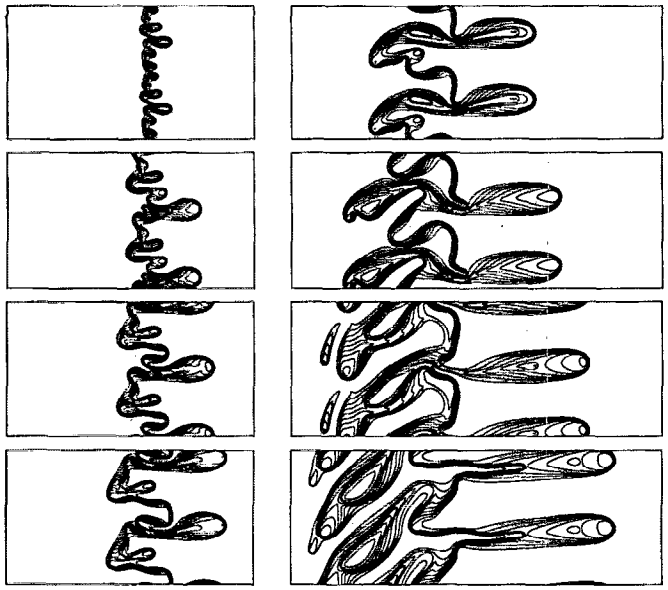

FIG. 15. Concentration contours for Pe=500, $R=3$, $S=0$, and moderate tangential shear, $|V_1-V_2|=2.5(1-e^{-R})$. Two periods in the y direction are displayed. Diagonal fingering results in complicated interfacial folding that traps blobs of more viscous fluid in phase 1. Frames correspond to $t=300$, 500, 600, 700, 900, 1100, 1300, 1500.

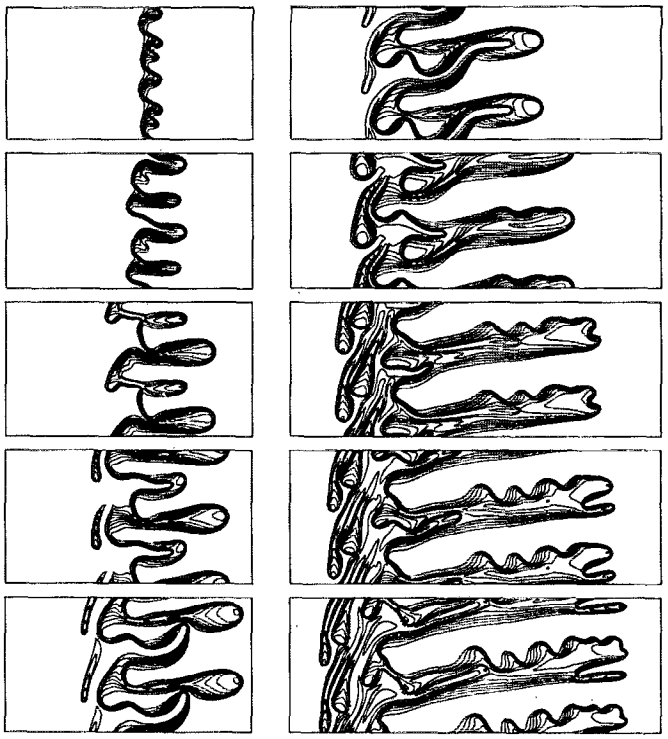

FIG. 16. Concentration contours for Pe=500, $R=3$, $S=0$, and strong tangential shear, $|V_1-V_2|=5(1-e^{-R})$. Two periods in the y direction are displayed. Notice the repeated detachment of trailing lobes and the development of a secondary side-finger instability. Frames correspond to $t=500$, 700, 900, 1000, 1100, 1200, 1400, 1600, 1700, 1800.

D. Comparison of long-term interfacial evolution with varying tangential shear

The presence and strength of tangential velocities strongly influences the overall evolution of the interface. As we demonstrated earlier, the growth and width of the emerging fingers are affected and new dynamics are possible. We would now like to illustrate how the presence of tangential velocities, through the fingering mechanisms described above, affects the long-term development of the interface.

Consider again the set of simulations shown in Fig. 5 at early times, in which Pe=500, $R=3$, and $S=0$. Figure 14 shows the long-term evolution of the interface when there are no global tangential velocities. This simulation is characterized by horizontal fingers that interact through the mechanisms of fading (frame 5) and coalescence (frame 11), as well as shielding and pairing.

The dynamics of the interface changes dramatically when tangential shearing velocities are present. The simulation corresponding to $(V_1,V_2)=(2.5,0.125)$ is shown in Fig. 15. Two periods in the y direction are displayed. In frame 1 we see that five fingers per period have developed as a result of shielding and spreading. By frame 2, coalescence has assisted in reducing the number of fingers to three. As one finger spreads and partially coalesces with the dominant finger (frame 5), the smallest finger fades (frames 3 and 4). The orientation and steepness of the interface near the fading finger, however, results in diagonal fingering due to the displacement velocity $(U,V_1)=(1,2.5)$. This fingering not only pushes through the remains of the fading finger (frame 5) but also through the under side of the dominant finger (frame 6), trapping a pool of fluid 2 in the upstream diagonal lobe. Another coalescing of the front into the horizontal fingers occurs (frame 6), while the diagonal fingering continues to progress, producing an interface which is quite complicated. Meanwhile, a lip at the end of the diagonal lobe is created, and a smaller trailing lobe forms and detaches due to V_1 (frames 6–8). The folding of the interface and advancement of the diagonal fingers results in another pocket of fluid 2 trapped in the upstream diagonal lobe (frame 7). The diagonal fingering then splits, with one stream of fluid 1 replenishing the horizontal finger which has almost pinched off (frame 8), while the other stream begins to break through the diagonal lobe. We assume that this stream will then isolate the diagonal lobe in fluid 1, and contribute to the growth of the horizontal fingers as the tangential velocity transitions from the high velocity V_1 to the relatively small velocity V_2.

Figure 16 shows the evolution of the interface for stronger tangential shearing, $(V_1,V_2)=(5.0,0.25)$. Again, two periods in the y direction are displayed. By frame 2, shielding and pairing have left two dominant fingers and a lip has formed at the root of one. Diagonal fingering directed at this part of the interface begins to choke (frame 3) and then replenish (frame 4) the smaller finger. Meanwhile, a trailing lobe is formed and quickly detaches due to the large velocity $V_1=5$ (frames 3 and 4). The replenished finger coalesces with the other (frames 5 and 6) to form one dominant finger that then grows diagonally. The secondary side-finger instability sets in on the upper side of

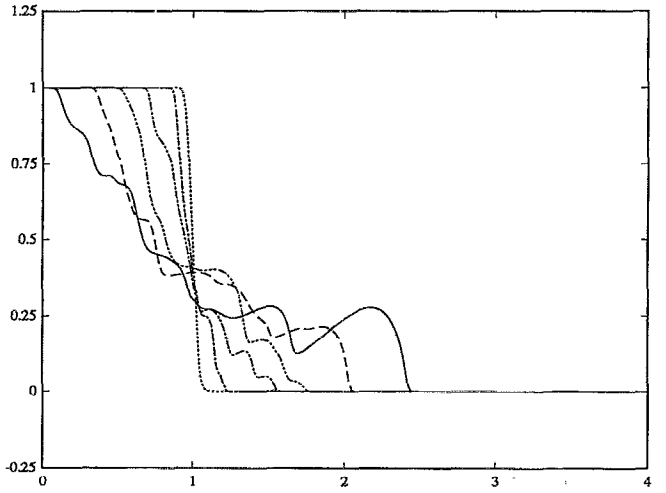

FIG. 17. y-averaged concentration profiles for the simulation shown in Fig. 14 (Pe=500, $R=3$, $S=0$, $V_1=V_2=0$). The profile is typical of horizontal fingering patterns. Profiles shown correspond to times $t=100$, 200, 400, 600, 800, 1000.

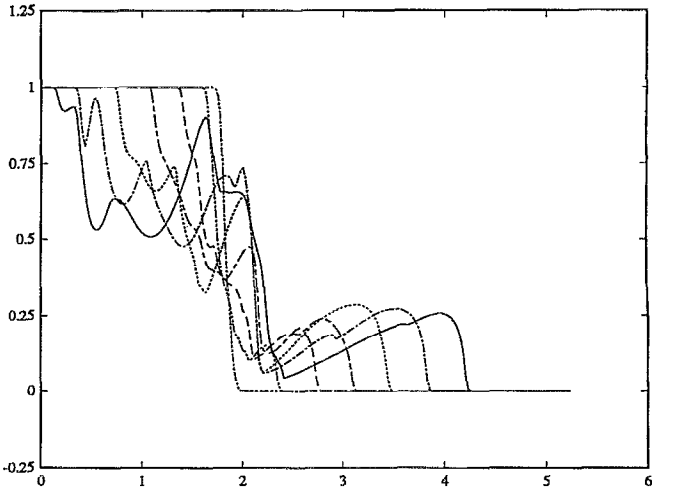

FIG. 18. y-averaged concentration profiles for the simulation shown in Fig. 15 [Pe=500, $R=3$, $S=0$, $|V_1-V_2|=2.5(1-e^{-R})$]. Interfacial folding results in local maxima near the center of the front while the detachment of trailing lobes is represented by the trough at the back of the profile. Profiles shown correspond to times $t=200$, 400,...,1400.

the finger (frame 7) since this side is viscously unstable to the velocity V_2 which is directed in the $+y$ direction. As we saw before, the side-finger instability leads to a widening of the tip which consequently splits (frames 7 and 8). As the perturbations on the finger side amplify, the finger continues to grow and another tip-splitting event begins (frame 10). Meanwhile, the diagonal fingering at the back repeatedly replenishes the dominant finger and detaches blobs of more viscous fluid at the root.

In these examples we have demonstrated how the presence of global tangential velocities has lead to new characteristics of the interfacial evolution. In addition to the mechanisms of shielding, pairing, fading, coalescence, and tip splitting, we now have the possibility for diagonal fingering, secondary side-finger instability, and trailing-lobe detachment. These new mechanisms further complicate the development of the interface that is often characterized by a greater degree of coalescence and interfacial folding, and by the repeated detachment and isolation of fluid blobs in the other phase.

E. One-dimensional averages

We can characterize the fingering in a one-dimensional profile by averaging the concentration field in the transverse direction. Figure 17 shows the y-averaged concentration at various times for the simulation shown in Fig. 14. Because this simulation is one in which there are no tangential velocities, the y-averaged profile displays the same characteristics typical of horizontal fingering patterns. As discussed in Refs. 7, 9, and 11, initially we see small deviations from the purely diffusive profile as the interface destabilizes. As fingering begins, peaks corresponding to the fingers are evident in the profile. These localized peaks vary as time progresses, reflecting the competitive growth and nonlinear interaction of the fingers. At the final time, there are two dominant humps on the downstream side of the interface, corresponding to the two fingers in the last frame of Fig. 14. The sharp drops in the profile on the downstream side of each hump illustrate the fact that there are steep gradients at the finger tips.

In Fig. 18, the y-averaged profiles are displayed for the simulation shown in Fig. 15 in which tangential shearing velocities are present. At later times, the downstream part of the profile shows the single dominant hump characterizing the horizontal finger in Fig. 15. As we saw in Fig. 15 however, diagonal fingering due to nonzero tangential velocities created an interface in which blobs of more viscous fluid became encircled by the less viscous displacing fluid. This is reflected in the y-averaged profiles by the local maxima and minima present on the upstream half of the profile. The local maximum near the center of the front grows as time increases, representing the advancement of fluid 1 (with concentration $c=1$) diagonally through the mixing zone while the diagonal downstream lobes, composed of low-concentration fluid, fade. We can also see the mark of the trailing-lobe detachment, represented by the trough at the back of the profile.

The troughs corresponding to the trailing-lobe detachment are even more evident in Fig. 19, showing the y-averaged profiles corresponding to the strong tangential shearing simulation in Fig. 16. Also notice, however, that the profile no longer exhibits a single dominant hump, even though only one finger is present on the downstream end of the simulation flow. Instead, the downstream ridge of the y-averaged profile, representing the single finger, shows oscillations. This is a result of the side-finger instability, and indicates how the average concentration across the finger varies due to the amplifying perturbation on the finger side.

A quantity of interest is the measure of the region where the two fluids mix. Although the length of the mixing zone can be defined in a number of ways, we choose to

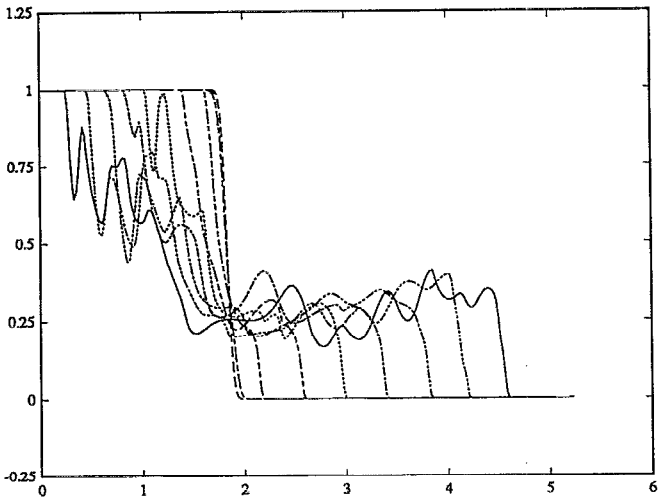

FIG. 19. y-averaged concentration profiles for the simulation shown in Fig. 16 [Pe=500, $R=3$, $S=0$, $|V_1-V_2|=5(1-e^{-R})$]. The side-finger instability is evident as oscillations on the downstream ridge of the profile, while multiple troughs at the back represent the repeated trailing-lobe detachments. Profiles shown correspond to times $t=200, 400,\ldots,1800$.

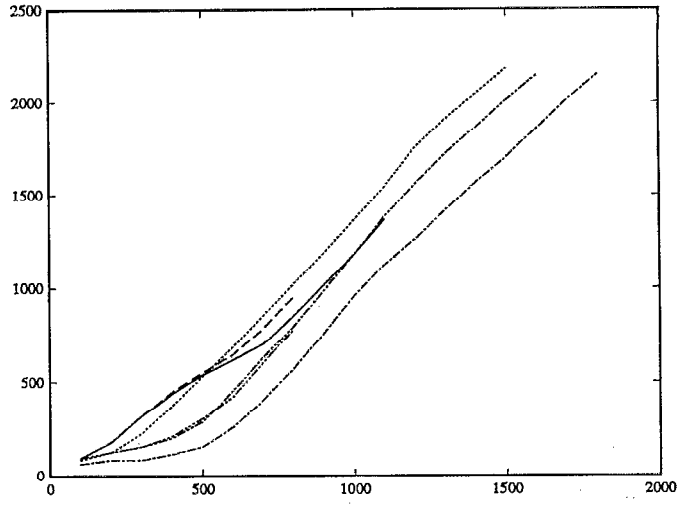

FIG. 20. Mixing lengths vs time for a variety of simulations corresponding to $R=3$ and Pe=500. (Solid curve) $S=0$, $|V_1-V_2|=0$. (Dot–dot) $S=0$, $|V_1-V_2|=2.375$. (Dot–dash) $S=0$, $|V_1-V_2|=4.75$. (Dot–dot–dash) $\theta=0$, $|V_1-V_2|=4.2$, ($S=1$, $G=1$). (Dot–dot–dot–dash) $\theta=0$, $|V_1-V_2|=1.45$, ($S=4$, $G=1$). (Dash–dash) $\theta=0$, $|V_1-V_2|=0.1$, ($S=-1$, $G=1.5$). Despite the variation in tangential shear strength, the same asymptotic mixing rate, 1.5, is achieved.

simply compute it from the y-averaged concentration profile. Specifically, we take

$$\mathscr{L}_{\text{mix}}=|x(c=0.975)-x(c=0.025)|. \tag{45}$$

The mixing length for a stable front has a $t^{1/2}$ dependence since

$$c_b(x,t)=\frac{1}{2}\operatorname{erfc}\left(\frac{x-t}{2\sqrt{t}}\right). \tag{46}$$

As Zimmerman and Homsy[9] point out, the mixing length for an unstable front may also behave initially as $t^{1/2}$ even when fingering is visible, provided the initial perturbation is small. As the fingering takes hold and progresses, the mixing length increases linearly with time and grows at a nearly constant rate. Zimmerman and Homsy[9] also found that, at high Péclet number, the rate of growth of the mixing zone is independent of the Péclet number. For a viscosity contrast corresponding to $R=3$, they found this asymptotic mixing rate to be approximately 1.5. In a later investigation, Zimmerman and Homsy[11] quantified the intuitive result that well-developed fingers grow more quickly when the viscosity contrast increases by demonstrating that the mixing rate increases monotonically with R. For the flow we are considering, the effect of density contrast, angle of inclination, and tangential velocities on the mixing rate is also of interest. We first focus on the effect of tangential shearing velocities. Figure 20 shows mixing lengths for a variety of simulations as a function of time. Each of the simulations represented corresponds to either $S=0$ or $\theta=0$ to isolate the effect of the tangential velocities. For each case, $R=3$ and Pe=500 but the tangential shear strength varies. In cases where the tangential shear is strong, the dispersive behavior continues for longer times since the growth of fingers is slowed due to the increased stabilization of the flow. In some cases, competition between fingers results in multiple fading events and the growth of the mixing zone is temporarily slowed somewhat. However, the mixing length eventually increases at a nearly constant rate. Despite the variation in tangential shear strength and the new fingering dynamics that are introduced, the same rate of growth is achieved. This asymptotic mixing rate is approximately 1.5, in agreement with the rate found by Zimmerman and Homsy for $R=3$ when there are no global tangential velocities.

To study the influence of buoyancy on the asymptotic mixing rate, we consider a horizontal interface with gravity directed from fluid 1 to fluid 2 ($\theta=\pi/2$), and consider the no-shear case $V_1=V_2=0$. Taking $G=1$, the instability criterion formulated in Ref. 1 and given in Eq. (32) reduces to

$$R-S\frac{(1+e^S)}{(1+e^R)}>0. \tag{47}$$

This flow becomes more stable as $S=\ln(\rho_2/\rho_1)$ increases and is neutrally stable for $S=R$. In Table I the asymptotic mixing rates for a series of simulations with various buoyancy conditions are cataloged. The increased stability of

TABLE I. Asymptotic mixing rates for various buoyancy conditions. The flow becomes more stable as S increases and the growth of the mixing zone is slowed. Pe=500, $R=3$, $G=1$, $\theta=\pi/2$, $V_1=V_2=0$.

S	Mixing rate, $\frac{d}{dt}(\mathscr{L}_{\text{mix}})$
0.0	1.50
1.5	1.16
2.0	0.76
2.5	0.50

the flow due to stable density stratification, like that due to the tangential shearing velocities, slows the emergence of fingers. However, Table I shows that unlike the tangential shear case increased stabilization by buoyancy effects does lower the asymptotic mixing rate.

In summary, the new mechanisms that arise from the presence of tangential velocities alter the cartoon of the average fingering profile but do not affect the asymptotic mixing rate. Although the efficiency of the displacement cannot be improved by tangential shear, increasing the stability of the interface by favorable density stratification does reduce the rate of growth of the mixing zone.

F. Nonexponential density–concentration relationships

In the results we have presented so far, we have assumed the viscosity and density relations,

$$\mu(c)=e^{R(1-c)}, \quad \rho(c)=e^{S(1-c)}. \tag{48}$$

In an effort to isolate the effect of tangential velocities, we have often considered the constant-density case ($S=0$) in our simulations of the nonlinear dynamics. Nonetheless, the functional relationships of the viscosity and density with respect to the concentration are of fundamental importance to both the stability and dynamics of the interfacial evolution. Our purpose here will be to illustrate the differences in the evolution of interface when the functional dependence of concentration on density is varied. We still take the viscosity to be exponentially varying

$$\mu(c)=e^{R(1-c)}, \tag{49}$$

but consider four density relations,

$$\rho_e(c)=e^{S(1-c)}, \tag{50}$$

$$\rho_l(c)=(e^S-1)(1-c)+1, \tag{51}$$

$$\rho_{a_1}(c)=(e^S-1)(1-c)^{\alpha}+1, \tag{52}$$

$$\rho_{a_2}(c)=(e^S-\beta-1)(1-c)^{\alpha}+\beta(1-c)+1. \tag{53}$$

The coefficients for the exponential, ρ_e, linear, ρ_l, and algebraic, ρ_{a_1} and ρ_{a_2}, relations have been selected so that in all four cases,

$$\rho_1=\rho(c=1)=1, \tag{54}$$

$$\rho_2=\rho(c=0)=e^S, \tag{55}$$

keeping the densities of the two fluids constant as we vary the density in the mixed region.

For simplicity, consider the case of a horizontal interface, with $\theta=\pi/2$, so the flow is gravitationally stable when $\rho_1<\rho_2$. When the density varies exponentially, $\rho=\rho_e$, this flow is unstable when

$$R-GS\frac{(1+e^S)}{(1+e^R)}>0 \tag{56}$$

or

$$R>S \quad \text{for } G=1. \tag{57}$$

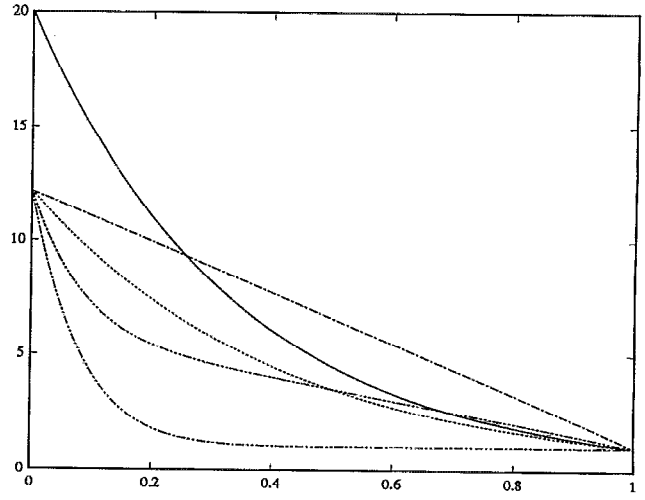

FIG. 21. Exponentially varying viscosity and four density relations as a function of concentration for $R=3$ and $S=2.5$. Exponential viscosity, $\mu(c)=e^{R(1-c)}$ (solid curve), exponential density, $\rho_e(c)=e^{S(1-c)}$ (dot–dot), linear density, $\rho_l(c)=(e^S-1)(1-c)+1$ (dot–dash), algebraic density case 1, $\rho_{a_1}(c)=(e^S-1)(1-c)^{12}+1$ (dot–dot–dash), algebraic density case 2, $\rho_{a_2}(c)=(e^S-6)(1-c)^{12}+5(1-c)+1$ (dot–dot–dot–dash).

We consider the case $R=3$, $S=2.5$ (with $G=1$, $\theta=\pi/2$, Pe=500), and focus on the effect of the density distribution by considering only the zero tangential velocity case. The viscosity and four density relations for $R=3$ and $S=2.5$ are plotted in Fig. 21 as a function of the concentration. In the algebraic cases, we have taken $\alpha=12$ and $\beta=5$. As we can see from Eq. (20), it is the variation of the density, $d\rho/dc$, in comparison with that of the viscosity, $d\mu/dc$, that dictates the stability and dynamics of the flow. The magnitude of these functions is plotted in Fig. 22. In

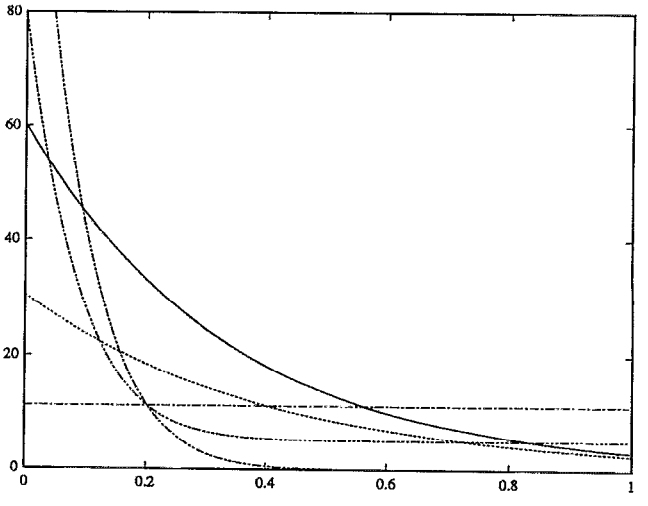

FIG. 22. $|d\mu/dc|$ and $|d\rho/dc|$ versus concentration for $R=3$ and $S=2.5$. Exponential viscosity, $\mu(c)=e^{R(1-c)}$ (solid curve), exponential density, $\rho_e(c)=e^{S(1-c)}$ (dot–dot), linear density, $\rho_l(c)=(e^S-1)(1-c)+1$ (dot–dash), algebraic density case 1, $\rho_{a_1}(c)=(e^S-1)(1-c)^{12}+1$ (dot–dot–dash), algebraic density case 2, $\rho_{a_2}(c)=(e^S-6)(1-c)^{12}+5(1-c)+1$ (dot–dot–dot–dash).

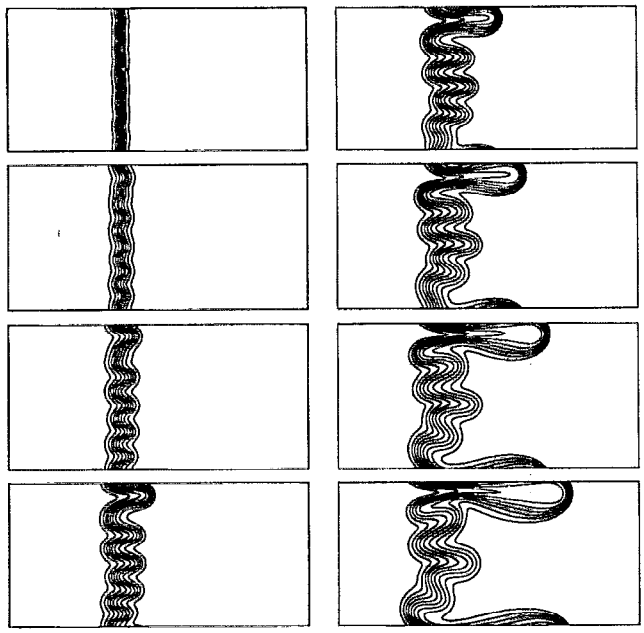

FIG. 23. Concentration contours for exponential density relation, $\rho(c)=\rho_e(c)$, for which the flow is globally unstable. Pe=500, $R=3$, $S=2.5$, $G=1$, $\theta=\pi/2$, $V_1=V_2=0$. Frames correspond to $t=200$, 400,...,1600.

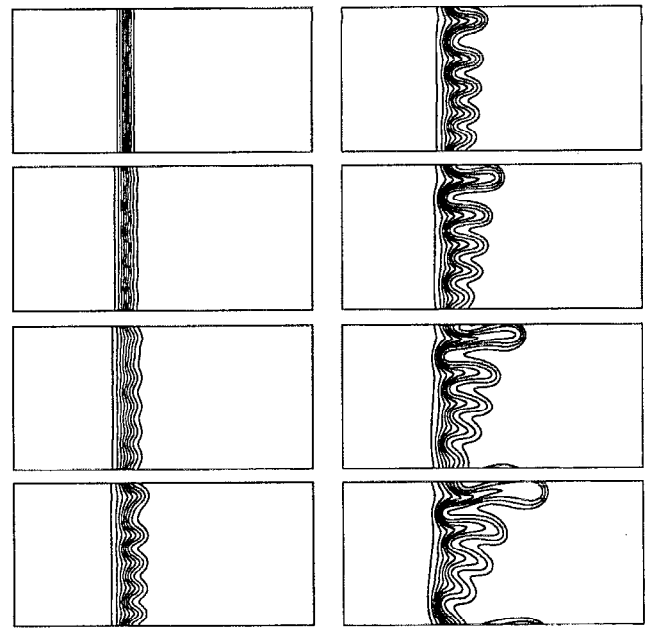

FIG. 24. Concentration contours for linear density relation, $\rho(c)=\rho_l(c)$, for which the flow is locally stable on the upstream half of the interface. Pe=500, $R=3$, $S=2.5$, $G=1$, $\theta=\pi/2$, $V_1=V_2=0$. Frames correspond to $t=200$, 400,...,1600.

this configuration and with an exponential density relation, the flow is neutrally stable for $R=S$, so that $|d\rho/dc| = |d\mu/dc|$. When S is less than R, as in Fig. 22, and the density relation is exponential, then $|d\rho/dc| < |d\mu/dc|$ for all values of c. Since the instability criterion is satisfied throughout the mixed region, we refer to this flow as *globally unstable*. However, when the density varies linearly with the concentration, $|d\rho/dc| < |d\mu/dc|$ for only some values of c, $0 \leqslant c < 0.56$ in this case. This flow is *locally unstable* since density effects tend to stabilize the flow at high concentration levels. In Figs. 23 and 24 concentration contours for the evolution of the interface are shown for the exponential and linear density relations, respectively. The interfacial evolution corresponding to the exponential case, $\rho(c)=\rho_e(c)$, exhibits characteristics typical of the horizontal fingering we have seen before when there are no tangential velocities. Perturbations at the interface amplify at all concentration levels and macroscopic fingers emerge. A dominant finger develops, with steep concentration gradient at the tip. As this finger grows, it spreads at the tip, shielding adjacent fingers. In contrast, Fig. 24 corresponding to the linear case, $\rho(c)=\rho_l(c)$, shows quite a different scenario. Since this flow is only locally unstable for low concentration levels, or mixtures composed mostly of fluid 2, the growth of perturbations is localized to the downstream half of the interface. The upstream side, which is linearly stable, maintains a nearly one-dimensional profile even as macroscopic fingers emerge. At later times, the linearly stable region is perturbed by strong nonlinear effects due to the presence of well-developed fingering. The stability of the upstream half of the interface can be further illustrated by calculating the upstream and downstream mixing lengths. We define these mixing lengths as

$$\mathscr{L}^{+}_{\text{mix}} = |x(c=0.975) - x_1|, \tag{58}$$

$$\mathscr{L}^{-}_{\text{mix}} = |x_1 - x(c=0.025)|, \tag{59}$$

where x_1 is the initial location of the center of the front. As can be seen in Fig. 25, the upstream mixing length $\mathscr{L}^{+}_{\text{mix}}$ follows the base-flow behavior of $2(2t)^{1/2}$. The presence of this locally stable region also affects the fingering in the

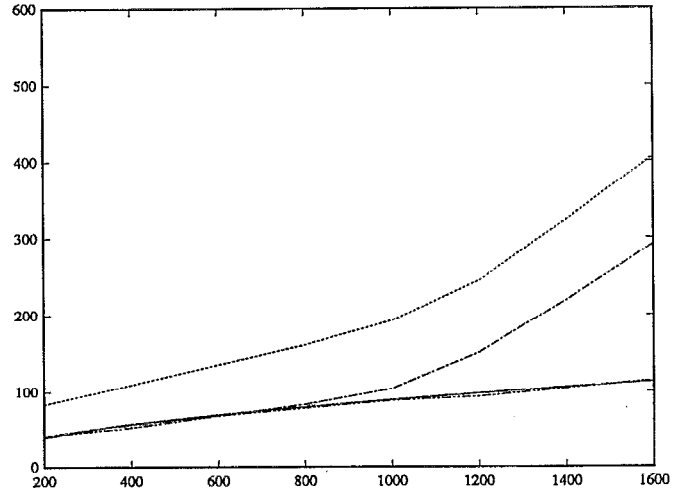

FIG. 25. Mixing lengths for simulation shown in Fig. 24 with linear density relation, $\rho(c)=\rho_l(c)$. Base-state behavior $2(2t)^{1/2}$ (solid curve), $\mathscr{L}_{\text{mix}}=\mathscr{L}^{+}_{\text{mix}}+\mathscr{L}^{-}_{\text{mix}}$ (dot–dot), downstream component $\mathscr{L}^{-}_{\text{mix}}$ (dot–dash), upstream component $\mathscr{L}^{+}_{\text{mix}}$ (dot–dot–dash).

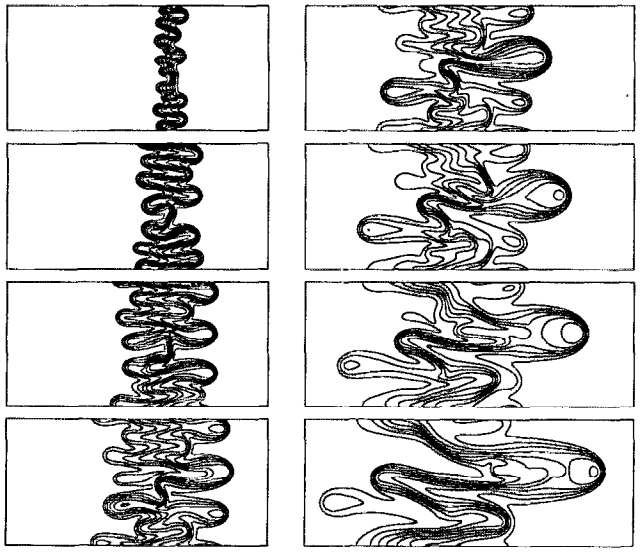

FIG. 26. Concentration contours for the first algebraic density relation, $\rho(c) = \rho_{a_1}(c)$, for which the flow is locally stable in a small region on the downstream edge of the interface. Pe=500, $R=3$, $S=2.5$, $G=1$, $\theta=\pi/2$, $V_1=V_2=0$. Frames correspond to $t=200, 400,...,1600$.

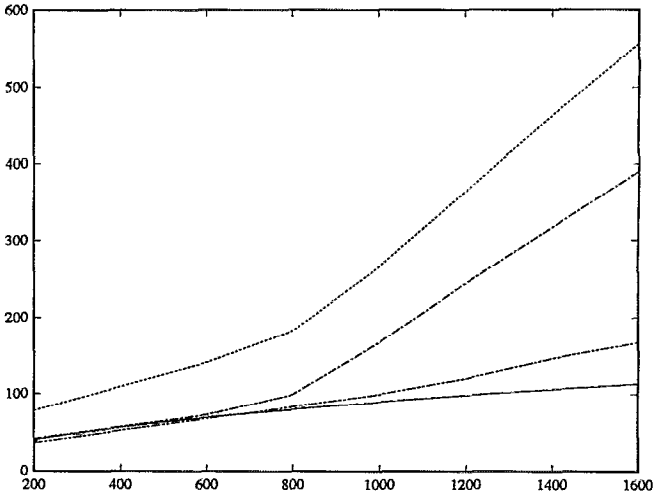

FIG. 28. Mixing lengths for simulation shown in Fig. 23 with exponential density relation, $\rho(c)=\rho_e(c)$. Base-state behavior $2(2t)^{1/2}$ (solid curve), $\mathscr{L}_{\text{mix}}=\mathscr{L}^{+}_{\text{mix}}+\mathscr{L}^{-}_{\text{mix}}$ (dot–dot), downstream component $\mathscr{L}^{-}_{\text{mix}}$ (dot–dash), upstream component $\mathscr{L}^{+}_{\text{mix}}$ (dot–dot–dash).

unstable region. The stable region acts to prevent the penetration of fluid 1, resulting in fingers that are more diffuse and grow slower. These more diffuse fingers have a weaker associated cross-flow, so the dominant finger in Fig. 24 does not spread as readily, and shielding of adjacent fingers is inhibited. Weakened by the stable region upstream, the extent of finger interactions is reduced and the overall evolution of the interface is simplified.

The development of the interface when the density varies algebraically with the concentration is shown in Fig. 26 for the first algebraic case, $\rho(c) = \rho_{a_1}(c)$. Figure 22 shows that in this case $|d\rho/dc| < |d\mu/dc|$ except for values of c near zero, representing mixtures composed mostly of fluid 2. Because the range of c for which the flow is linearly stable is relatively small, we do not readily see a stable region in the nonlinear simulation shown in Fig. 26. However, the evolution of the interface still differs from what we would expect when the instability is global. Because the difference between $|d\rho/dc|$ and $|d\mu/dc|$ in the unstable region is greater in this case than in the exponentially dependent case (Fig. 21), the interface destabilizes more quickly and more fingers emerge. If the interface were globally unstable we would expect the fingers in frame 3 that have edged out in front to grow explosively and quickly shield the neighboring fingers. Instead, the modest barrier created by the stable region downstream inhibits the growth of the fingers. Fluid 1 does flow preferentially through one of the fingers, steepening the concentration gradient, but the selected finger is discouraged from advancing rapidly ahead of its neighboring fingers. This effect can be seen in the mixing lengths, $\mathscr{L}^{+}_{\text{mix}}$ and $\mathscr{L}^{-}_{\text{mix}}$ plotted in Fig. 27. The fact that the downstream mixing length $\mathscr{L}^{-}_{\text{mix}}$ is reduced to that of $\mathscr{L}^{+}_{\text{mix}}$ for this case, should be contrasted with the behavior of the globally unstable exponential case, shown in Fig. 28, where the rapid growth of the fingers into the second phase is reflected in a larger rate of expansion of the downstream mixing zone. (We note that the combined mixing length, $\mathscr{L}_{\text{mix}}$, for these simulations does not grow at the rate 1.5 even though $R=3$ since gravitational forces increase the stability of the flow.) In more extreme cases, with a larger downstream region of stability, we might expect the fingering into fluid 2 to be severely limited, with the opposite effect of that shown in Fig. 24.

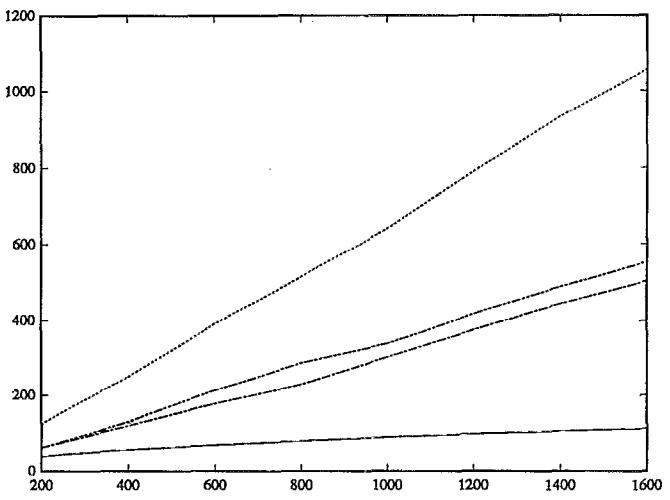

FIG. 27. Mixing lengths for simulation shown in Fig. 26 with algebraic density relation, $\rho(c) = \rho_{a_1}(c)$. Base-state behavior $2(2t)^{1/2}$ (solid curve), $\mathscr{L}_{\text{mix}}=\mathscr{L}^{+}_{\text{mix}}+\mathscr{L}^{-}_{\text{mix}}$ (dot–dot), downstream component $\mathscr{L}^{-}_{\text{mix}}$ (dot–dash), upstream component $\mathscr{L}^{+}_{\text{mix}}$ (dot–dot–dash).

The last case we consider is that of the second algebraically varying density relation, $\rho(c) = \rho_{a_2}(c)$. As Fig. 22 shows, in this case $|d\rho/dc| < |d\mu/dc|$ for an intermediate range of concentration levels so that the flow is locally stable in two small regions on the upstream and downstream edges of the interface. As with the first algebraic case, these small regions of stability are not evident in the

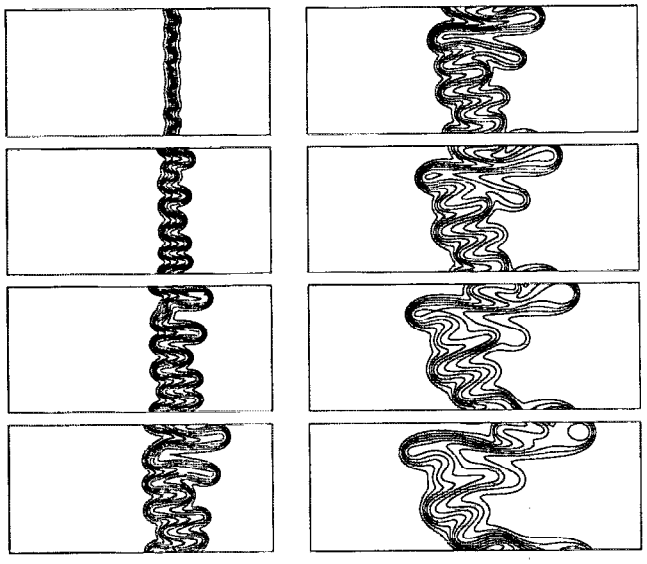

FIG. 29. Concentration contours for the second algebraic density relation, $\rho(c) = \rho_{a_2}(c)$, for which the flow is locally stable in two small regions on the upstream and downstream edges of the interface. Pe=500, $R=3$, $S=2.5$, $G=1$, $\theta=\pi/2$, $V_1=V_2=0$. Frames correspond to $t=200$, 400,...,1600.

nonlinear simulation shown in Fig. 29. In comparing this simulation with that for the first algebraic case (Fig. 26), we see that the early evolution is somewhat similar but the "back fingering" seen in Fig. 26 is inhibited in this case by the locally stable region upstream. Fingering is discouraged both upstream and downstream by the locally stable regions. The corresponding mixing lengths in Fig. 30 show $\mathscr{L}^-_{\rm mix} > \mathscr{L}^+_{\rm mix}$ as *both* downstream and upstream mixing lengths are reduced. Overall, the algebraic cases illustrate that even small regions of localized stability can significantly alter the evolution of the interface. In both cases,

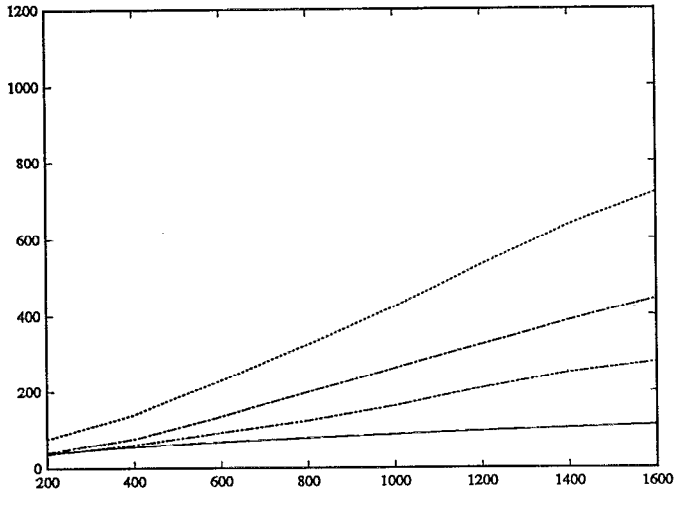

FIG. 30. Mixing lengths for simulation shown in Fig. 29 with algebraic density relation, $\rho(c) = \rho_{a_2}(c)$. Base-state behavior $2(2t)^{1/2}$ (solid curve), $\mathscr{L}_{\rm mix}=\mathscr{L}^+_{\rm mix}+\mathscr{L}^-_{\rm mix}$ (dot–dot), downstream component $\mathscr{L}^-_{\rm mix}$ (dot–dash), upstream component $\mathscr{L}^+_{\rm mix}$ (dot–dot–dash).

fingers are discouraged from advancing quickly into the second phase, so the shielding mechanism does not take place as easily. The shielding mechanism plays a fundamental role in finger interactions so there is less interplay in Figs. 26 and 29 than we would expect when the flow is globally unstable. Once a preferred finger is selected, the primary mechanism by which the number of fingers is reduced in these locally unstable cases is diffusion.

In these few examples, we have illustrated how the nature of the interfacial evolution can be altered by varying the density–concentration relation. Both the degree of instability and the region of instability can change, resulting in a variation in the number of fingers that emerge, the mechanisms by which they develop, and the level of finger competition. Given the results presented here, it is clear that further investigation would be of interest to study the interfacial dynamics for nonmonotonic density relations as well as nonexponential viscosity relations. Studies of nonmonotonic viscosity profiles for the neutrally buoyant case have recently produced some very interesting results.[17]

IV. CONCLUSION

Our results indicate that the nonlinear evolution of the interface possesses new characteristics when global tangential velocities are present. Tangential shearing not only alters the wavelength and growth of the emerging fingers, as predicted by the linear stability analysis, but also affects the shape and concentration distribution of the fingers. In addition to the finger mechanisms of shielding, pairing, fading, coalescence, and tip splitting, we have identified the new mechanisms of diagonal fingering, trailing-lobe detachment, and secondary side-finger instability. The dynamics resulting from these new mechanisms often lead to a more complicated interfacial evolution than previously reported. On the other hand, we find that the asymptotic mixing rate does not vary with tangential shear strength, although initially the mixing zone spreads more slowly as the strength of the tangential shear increases. The mixing rate can be reduced, thereby increasing the efficiency of the displacement, by increasing the stability of the flow through buoyancy effects.

We have also performed a preliminary study that illustrates how the dynamics of the interface is sensitive to the density–concentration relation, particularly when the region of instability is localized. In the cases we have considered, the degree of finger interaction is reduced when the flow is only locally unstable, simplifying the overall evolution of the interface. However, we feel that other combinations of density and viscosity relations should be studied to further explore the influence of these relations on the stability and dynamics of the flow. We hope that the results we have presented on the influence of gravity and tangential velocities will encourage experimental work and enable the verification of our conclusions. We also hope that these effects will be included with those arising from permeability heterogeneity and anisotropic dispersion in future research efforts.

ACKNOWLEDGMENTS

We gratefully acknowledge support for this research by the National Science Foundation through Grant No. CTS-9196004, by the Eastman Kodak Company, by the Petroleum Research Fund, administered by the American Chemical Society, through Grant ACS-PRF No. 23284-G7, and by the DARPA-URI. Computing resources were provided by the San Diego Supercomputer Center.

[1]A. Rogerson and E. Meiburg, "Shear stabilization of miscible displacement processes in porous media," Phys. Fluids A **5**, 1344 (1993).
[2]G. M. Homsy, "Viscous fingering in porous media," Annu. Rev. Fluid Mech. **19**, 271 (1987).
[3]P. G. Saffman and G. I. Taylor, "The penetration of a fluid into a porous medium or Hele-Shaw cell containing a more viscous fluid," Proc. R. Soc. London Ser. A **245**, 312 (1959).
[4]S. Hill, "Channelling in packed and columns," Chem. Eng. Sci. **1**, 247 (1952).
[5]R. L. Chuoke, P. von Meurs and C. van der Poel, "The instability of slow, immiscible, viscous liquid–liquid displacements in permeable media," SPE AIME Trans. **216**, 188 (1959).
[6]C. T. Tan and G. M. Homsy, "Stability of miscible displacements in porous media: Rectilinear flow," Phys. Fluids **29**, 3549 (1986).
[7]C. T. Tan and G. M. Homsy, "Simulation of nonlinear viscous fingering in miscible displacement," Phys. Fluids **31**, 1330 (1988).
[8]Y. C. Yortsos and M. Zeybek, "Dispersion driven instability in miscible displacement in porous media," Phys. Fluids **31**, 3511 (1988).
[9]W. B. Zimmerman and G. M. Homsy, "Nonlinear viscous fingering in miscible displacement with anisotropic dispersion," Phys. Fluids A **3**, 1859 (1991).
[10]C. T. Tan and G. M. Homsy, "Viscous fingering with permeability heterogeneity," Phys. Fluids A **4**, 1099 (1992).
[11]W. B. Zimmerman and G. M. Homsy, "Viscous fingering in miscible displacements: Unification of effects of viscosity contrast, anisotropic dispersion, and velocity dependence of dispersion on nonlinear finger propagation," Phys. Fluids A **4**, 2348 (1992).
[12]J.-C. Bacri, N. Rakotomalala, D. Salin and R. Wouméni, "Miscible viscous fingering: Experiments versus continuum approach," Phys. Fluids A **4**, 1611 (1992).
[13]M. Zeybek and Y. C. Yortsos, "Long waves in parallel flow in Hele–Shaw cells," Phys. Rev. Lett. **67**, 1430 (1991).
[14]M. Zeybek and Y. C. Yortsos, "Parallel flow in Hele–Shaw cells," J. Fluid Mech. **241**, 421 (1992).
[15]C. Canuto, M. Y. Hussaini, A. Quarteroni and T. A. Zang, *Spectral Methods in Fluid Dynamics*, Springer series in Computational Physics (Springer-Verlag, New York, 1988).
[16]C.-W. Shu and S. Osher, "Efficient implementation of essentially non-oscillatory shock-capturing schemes, II," J. Comput. Phys. **83**, 32 (1989).
[17]O. Manickam and G. M. Homsy, "Stability of miscible displacements in porous media with nonmonotonic viscosity profiles," Phys. Fluids A **5**, 1356 (1993).